
Supplementary information

Intense Brillouin amplification in gas using hollow-core waveguides

In the format provided by the
authors and unedited

Supplementary Information for:
Intense Brillouin amplification in gas using hollow-core waveguides

Fan Yang,^{*,†} Flavien Gyger,^{*} and Luc Thévenaz[†]

^{*} These two authors contributed equally

[†] Corresponding authors: fanyang808@gmail.com; luc.thevenaz@epfl.ch

Ecole Polytechnique Fédérale de Lausanne (EPFL),
Group for Fibre Optics, Lausanne, Switzerland

Contents

S1	Dual intensity modulation	S1
S1.1	Introduction	S1
S1.2	System response	S2
S1.3	Experimental verification	S5
S1.4	Experimental Brillouin gain calculation	S6
S2	Detailed experimental set-up for signal amplification	S7
S3	Detailed experimental set-up for distributed temperature sensing	S8
S3.1	Dual intensity modulation implementation	S8
S3.2	PRBS generator	S9
S3.3	Phase modulator	S9
S3.4	Correlation location scanning	S9
S3.5	Pump power	S9
S3.6	Probe signal acquisition	S9
S3.7	Scanning, quadratic fitting and repeatability estimation	S9
S3.8	Test bench	S10
S4	Theoretical calculation of the Brillouin gain	S10
S5	Calculation of Raman gain coefficient	S11
S6	Acoustic velocity in CO ₂ at different gas pressures	S12
S7	Axial strain finite-element simulation	S13
S8	Response of a Mach-Zehnder intensity modulator	S14
S8.1	Introduction	S14
S8.2	Intensity at a photodetector	S16
S8.3	Analysis of the three bias configurations	S17

S1 Dual intensity modulation

S1.1 Introduction

When measuring the Brillouin gain in low-pressure gas, the peak gain is relatively low (e.g. in 1 bar CO₂, it is about $10^{-3} \text{ m}^{-1}\text{W}^{-1}$ in our HCF). In this situation, the pump reflection at the SMF-HCF coupling interface, directly entering into the detector, is the source of fluctuations screening the gain to be measured. This reflection issue is resolved by introducing a dual intensity modulation at frequency $f_S/2$ and $f_P/2$ on the probe and pump beam, respectively. The modulators are Mach-Zehnder modulators and their bias is set to suppress the carrier. As a consequence, the probe and pump light intensities are modulated at a frequency f_S and f_P , respectively. Since stimulated Brillouin scattering is a non-linear process involving the product of pump and probe powers, sum and difference of frequencies are generated. After Brillouin interaction with the pump inside the gas-filled hollow-core fibre (HCF), the probe intensity is detected and band-pass filtered at a frequency $f_\Delta = f_S - f_P$ using a lock-in amplifier. Hence, the pump beam directly reaching the detector is filtered out in the radio frequency (RF) domain, since the detection is made at a frequency very distant

from f_P ^a. The experimental set-up is illustrated in Fig. S1. Note that the frequency difference, f_Δ , should remain much smaller than the Brillouin linewidth to secure steady-state acoustic waves. A similar technique is used to filter out stray light in Brillouin microscopy [1].

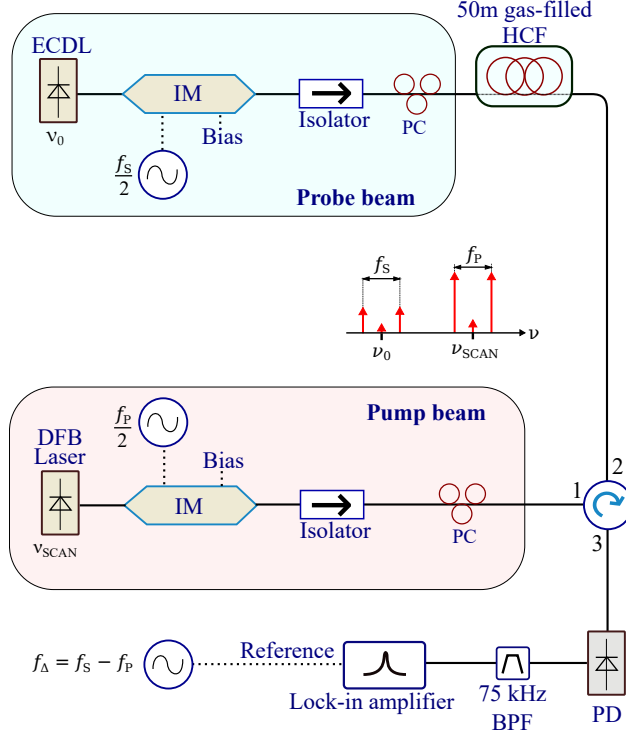


Figure S1: **Dual intensity modulation (DIM) experimental set-up.** Experimental set-up for Brillouin gain spectrum measurement using an intensity modulation for both pump and probe beams. Detection is performed at the frequency difference. Note that the three radio-frequency sources are synchronised to the same frequency standard. ECDL, external-cavity diode laser; DFB laser, distributed feedback laser; IM, intensity modulator; PC, polarisation controller; PD, photodetector; BPF, band-pass filter.

S1.2 System response

In this derivation, it is assumed that both intensity modulation frequencies f_S and f_P are much smaller than the Brillouin frequency shift ν_B . Moreover, the frequency difference $f_P - f_S$ is assumed to be much smaller than the Brillouin linewidth $\Gamma_B/2\pi$. Then, the acoustic wave governing the interaction at frequency f_Δ can be approximated to be at steady-state. Furthermore, absence of pump depletion is assumed. We assume the probe beam to co-propagate along the HCF (z-axis) and the pump beam to counterpropagate along the z-axis. In these conditions, the probe electric field amplitude along the z-axis, $E_s(z)$, in presence of stimulated Brillouin scattering, is governed by the following differential equation [2]:

$$\frac{\partial E_s}{\partial z} + \frac{n_g}{c} \frac{\partial E_s}{\partial t} = \frac{1}{2} g_B \mathcal{L}_A P_P E_s - \frac{\alpha}{2} E_s, \quad (1)$$

where g_B is the peak Brillouin gain, as defined in Eq. (1) in the main manuscript, c is the speed of light, n_g is the group refractive index of the fibre, α is the fibre loss in unit 1/m, $P_P(z) = P_{P0}e^{-\alpha(L-z)}$ is the pump

^aHowever, the reflection still needs to remain limited as to not damage the photodetector in the case of a high pump power. Furthermore, the photodetector may show a slight nonlinearity. In that case, the presence of both pump and probe beams at the detector could lead to sum-frequency difference generation within the detector itself, generating a background noise that may cover the desired signal. In our case, angled-cleaved SMFs are used to sufficiently reduce the reflection.

power along the HCF, P_{P0} being the input pump power at $z = L$, where L is the fibre length, and

$$\mathcal{L}_A(\Omega) = \frac{i\Omega\Gamma_B}{\Omega_B^2 - \Omega^2 + i\Omega\Gamma_B} \quad (2)$$

is the probe (amplification) field lineshape, for which the pump-probe detuning frequency $\Omega/2\pi = \nu_{\text{SCAN}} - \nu_0$, the Brillouin frequency shift $\nu_B = \Omega_B/2\pi$, and the Brillouin linewidth (full width at half maximum), $\Delta\nu = \Gamma_B/2\pi$, are defined. This definition assumes the probe wavelength to be larger than that of the pump beam (amplification side).

The equation is converted in units of power by using $P_S = A_{\text{eff}}\|E_s\|^2/2\eta$, where A_{eff} is the fibre effective area and η is the gas impedance:

$$\frac{1}{P_S} \left(\frac{\partial P_S}{\partial z} + \frac{n_g}{c} \frac{\partial P_S}{\partial t} \right) = g_B \mathcal{L}_I P_P - \alpha, \quad (3)$$

where $\mathcal{L}_I(\Omega) = \|\mathcal{L}_A(\Omega)\|^2$ is the intensity lineshape. In order to solve Eq. (3), we change the coordinate frame from (z, t) to (z', t') by performing the following change of variable:

$$\begin{aligned} z(z', t') &= z', \\ t(z', t') &= t' + \frac{n_g}{c} z'. \end{aligned} \quad (4)$$

Using these expressions for the original coordinates as a function of the new coordinates, we apply the chain rule and express:

$$\begin{aligned} \frac{\partial P_S(z, t)}{\partial z'} &= \frac{\partial P_S(z, t)}{\partial z} \frac{\partial z}{\partial z'} + \frac{\partial P_S(z, t)}{\partial t} \frac{\partial t}{\partial z'} = \frac{\partial P_S(z, t)}{\partial z} + \frac{n_g}{c} \frac{\partial P_S(z, t)}{\partial t}, \\ \frac{\partial P_S(z, t)}{\partial t'} &= \frac{\partial P_S(z, t)}{\partial z} \frac{\partial z}{\partial t'} + \frac{\partial P_S(z, t)}{\partial t} \frac{\partial t}{\partial t'} = \frac{\partial P_S(z, t)}{\partial t}. \end{aligned} \quad (5)$$

These expressions allow rewriting the partial differential equation, Eq. (3), as:

$$\frac{1}{P_S(z, t)} \frac{\partial P_S(z, t)}{\partial z'} = g_B \mathcal{L}_I P_P(z', t') - \alpha, \quad (6)$$

where the pump power P_P is now expressed as a function of the new coordinates. Since the time derivative disappears, it is now easier to solve the equation. An expression for the the pump power generated by the Mach-Zehnder modulator, $P_P(z, t)$, is derived in section S8. Using this derivation and the fact that the modulator bias is in carrier-suppressed configuration, P_P can be expressed as:

$$P_P(z, t) = \tilde{P}_{P0} e^{-\alpha(L-z)} \left(1 - \sum_n J_n(2\zeta_P) \cos(n(K_P z - \Omega_P t)) \right), \quad (7)$$

where $P_{P0} = \tilde{P}_{P0} (1 - J_0(2\zeta_P))$ is the time-averaged input pump power at the end of the HCF ($z = L$), $\Omega_P = \pi f_P$ and $K_P = -\Omega_P n_g/c$. We now transform this expression from (z, t) to the new coordinate frame, (z', t') . Given that the pump counter-propagates, $K_P < 0$, and the expression becomes:

$$P_P(z', t') = \tilde{P}_{P0} e^{-\alpha(L-z')} \left(1 - \sum_n J_n(2\zeta_P) \cos(n(2K_P z' - \Omega_P t')) \right), \quad (8)$$

which, to simplify subsequent integration, can also be expressed as:

$$P_P(z', t') = \tilde{P}_{P0} \left(e^{-\alpha(L-z')} - e^{-\alpha L} \text{Re} \left\{ \sum_n J_n(2\zeta_P) e^{(\alpha + 2inK_P)z' - in\Omega_P t'} \right\} \right). \quad (9)$$

Replacing pump power expression, Eq. (9) into Eq. (6) and integrating both sides along z' yields:

$$\begin{aligned} \ln \{P_S(z(z', t'), t(z', t'))\} \Big|_{z'=0}^{z'=L} &= \int_0^L (g_B \mathcal{L}_I P_P(z', t') - \alpha) dz' \\ &= \left(g_B \mathcal{L}_I \tilde{P}_{P0} \left(\frac{1}{\alpha} e^{-\alpha(L-z')} - e^{-\alpha L} \operatorname{Re} \left\{ \sum_n J_n(2\varsigma_P) \frac{e^{(\alpha+2inK_P)z' - in\Omega_P t'}}{\alpha + 2inK_P} \right\} \right) - \alpha z' \right) \Big|_{z'=0}^{z'=L}. \end{aligned} \quad (10)$$

Hence we obtain the general solution:

$$P_S(L, t) = P_S(0, t - n_g L/c) e^{-\alpha L} \exp \left(\tilde{P}_{P0} g_B \mathcal{L}_I L_{\text{eff}} \left(1 - \operatorname{Re} \left\{ \sum_n J_n(2\varsigma_P) \zeta_n e^{-in\Omega_P t} \right\} \right) \right), \quad (11)$$

where

$$L_{\text{eff}} = \frac{1 - e^{-\alpha L}}{\alpha} \quad (12)$$

is the fibre's effective length and

$$\zeta_n = \frac{1}{L_{\text{eff}}} \frac{\alpha - 2inK_P}{\alpha^2 + (2nK_P)^2} (e^{inK_P L} - e^{-inK_P L - \alpha L}) \quad (13)$$

is a modulation-dependent unitless parameter. The input probe power can be expressed as:

$$P_S(0, t - n_g L/c) = \tilde{P}_{S,0} \left(1 - \sum_m J_m(2\varsigma_S) \cos(m\Omega_S t + m\Phi_s) \right), \quad (14)$$

where $\Omega_S = \pi f_S$ is the modulation angular frequency, $P_{S,0} = \tilde{P}_{S,0} (1 - J_0(2\varsigma_S))$ is the time-averaged input probe power at $z = 0$, Φ_s contains both a phase shift between pump and probe modulations as well as the phase shift due to the probe propagation along the fibre. ς_S is the probe modulation depth. Section S8 gives a detailed derivation of intensity-modulated signals using a Mach-Zehnder modulator, including the definition of the modulation depth, ς . Since this technique was developed for the measurement of small Brillouin gains, we can now apply the small-gain approximation. After applying this approximation, the obtained expression consists of:

- A DC term.
- A term oscillating at multiples of the probe frequency, f_S .
- A term oscillating at multiples of the pump frequency, f_P .
- A term oscillating at multiples of the difference between the pump and probe frequencies, $f_S - f_P$.

As the detection is performed at the difference of the frequencies, only the last term is considered. The power in the small-gain approximation can then be written as:

$$P_{S,(\Omega_P \Omega_S)}(L, t) \cong -\tilde{P}_{S,\text{det}} \tilde{P}_{P0} g_B \mathcal{L}_I L_{\text{eff}} \operatorname{Re} \left\{ \sum_n \sum_m J_n(2\varsigma_P) J_m(2\varsigma_S) \zeta_n e^{-in\Omega_P t} \cos(m\Omega_S t + m\Phi_S) \right\}, \quad (15)$$

where $P_{S,\text{det}} = \tilde{P}_{S,\text{det}} (1 - J_0(2\varsigma_S))$ is the time-averaged probe power at detection. Since the lock-in amplifier only responds to the frequency difference $\Omega_\Delta = 2(\Omega_S - \Omega_P)$, only the terms $n = \pm 2, m = \pm 2$ are kept:

$$\begin{aligned} P_{S,\Omega_\Delta}(L, t) &\cong -2\tilde{P}_{S,\text{det}} \tilde{P}_{P0} g_B \mathcal{L}_I L_{\text{eff}} J_2(2\varsigma_S) J_2(2\varsigma_P) \\ &\quad \cdot \left(\cos(\Omega_\Delta t) (\operatorname{Re}\{\zeta_2\} \cos(2\Phi_S) + \operatorname{Im}\{\zeta_2\} \sin(2\Phi_S)) \right. \\ &\quad \left. + \sin(\Omega_\Delta t) (\operatorname{Re}\{\zeta_2\} \cos(2\Phi_S) + \operatorname{Im}\{\zeta_2\} \sin(2\Phi_S)) \right). \end{aligned} \quad (16)$$

The photoreceiver delivers a voltage equal to $V_{\text{det}} = \rho_{\text{pd}} P_{\text{det}}$, where ρ_{pd} is the power-to-voltage conversion factor. Then, in presence of a voltage signal of type $A \cos(\Omega t) + B \sin(\Omega t)$, the lock-in detection outputs the magnitude $\sqrt{A^2 + B^2}$, which gives:

$$V_{s,\text{det}} \cong \frac{2J_2(2\zeta_S)J_2(2\zeta_P)}{(1 - J_0(2\zeta_S))(1 - J_0(2\zeta_P))} \rho_{\text{pd}} P_{S,\text{det}} P_{P0} g_B \mathcal{L}_I L_{\text{eff}} \|\zeta_2\|. \quad (17)$$

The dependence of the set-up's response on the length and modulation frequency is given by the parameter:

$$\|\zeta_n\| = \frac{1}{L_{\text{eff}}} \sqrt{\frac{1 + e^{-2\alpha L} - 2e^{-\alpha L} \cos(2nK_P L)}{\alpha^2 + (2nK_P)^2}}. \quad (18)$$

The parameter ζ_n quantifies the interference effect occurring when the wavelength related to the modulation frequency f_P becomes comparable or smaller than the effective length of the fibre. That is, when the following condition: $\Lambda < L_{\text{eff}}$, where $\Lambda = c/(n_g f_P)$, is met, the system's response significantly decreases. On the contrary, when $\Lambda \gg L_{\text{eff}}$, the parameter $\zeta_n \approx 1$. Note that the pump beam is also attenuated by the probe beam. As a result, a π -phase shifted signal, co-propagating with the pump beam and of same magnitude as the one described above, is also generated. If the reflection of the HCF is too large (e.g. > -20 dB), then the reflection of this signal will interfere significantly with the main signal and this can be no longer neglected. In our case, the angled-cleaved SMF and the HCF connector generate < -36 dB reflection. We can therefore neglect the contribution from the pump reflection. Finally, note that in the special case of a bias at the quadrature-point for the two modulators (as used for the distributed temperature experimental set-up, section S3), the result given by Eq. (17) is modified to:

$$V_{s,\text{det},\text{QP}} \cong 2J_1(2\zeta_S)J_1(2\zeta_P)\rho_{\text{pd}} P_{S,\text{det}} P_{P0} g_B \mathcal{L}_I L_{\text{eff}} \|\zeta_1\|. \quad (19)$$

S1.3 Experimental verification

Here, we experimentally verify the set-up response provided by Eq. (17) and compare it with a single modulation set-up.

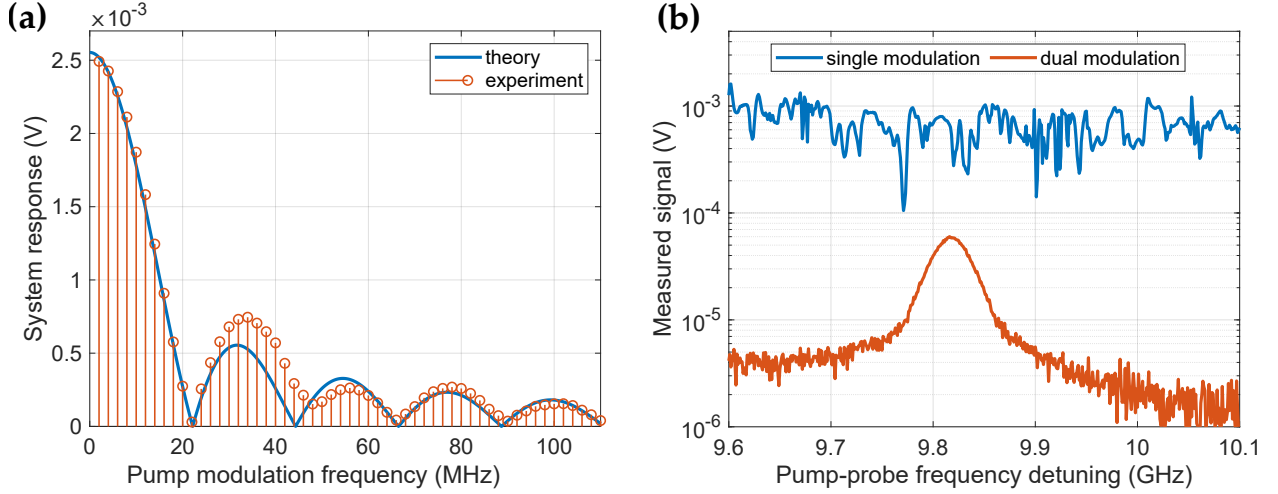


Figure S2: **Experimental verification of the dual intensity modulation method.** (a) Comparison of the measured system response with the calculated response given by Eq. (17), showing good qualitative agreement. (b) Comparison of the performances with the single modulation set-up in presence of a -48 dB reflection at the fibre coupling interfaces. In the case of the single intensity modulation method, the Brillouin gain signal is fully screened by the background fluctuations due to the pump reflection. By contrast, the signal from the dual intensity modulation method is not perturbed by this reflection and is able to accurately measure the gain.

System response

A 5-m-long standard ITU G.652 single-mode fibre was connected to the experimental set-up shown in Fig. S1 (replacing the gas-filled HCF with the 5-m-long SMF). Both pump and probe modulation frequencies

were gradually increased from 2 MHz to 110 MHz by 2 MHz steps, such that their difference, f_Δ , remained constant and equal to 75 kHz for the entire sequence. For each frequency step, the Brillouin gain was acquired and its peak value recorded. Figure S2(a) plots the results as a function of the pump modulation frequency, together with the theoretical curve obtained from Eq. (17), assuming a Brillouin gain of $g_B = 0.25 \text{ m}^{-1}\text{W}^{-1}$. We can observe that the measurements match well with the theoretical curve. Small deviations are observed and likely come from the presence of the connecting patchcords showing a slightly different Brillouin frequency shift.

Robustness to reflections

In order to verify the robustness of the dual intensity method against reflections, a 52-cm-long small-solid core fibre (ultra-high NA fibre with $1.8 \text{ }\mu\text{m}$ core diameter), with its both ends spliced to a single-mode fibre patchcords was used (i.e. replacing the gas-filled HCF with the small-core fibre in Fig. S1). This sample exhibits a reflection of -48 dB at the coupling interfaces caused by the effective index mismatch between the two fibre types. The gain of the second acoustic mode (high-order acoustic mode) of the small core fibre ($g_B \approx 0.062 \text{ m}^{-1}\text{W}^{-1}$) was measured using the single modulation set-up and the dual modulation set-up with the same parameters (same pump power, probe power and modulation depth). The time-averaged pump power, just before entering the sample, was 14 dBm and the detected probe power (time-averaged for the dual modulation case) was -8 dBm . The results are shown in Fig. S2(b). We can see that in the case of the single modulation, the pump reflection ($\approx -34 \text{ dBm}$) reaching the detector is sufficient to generate background fluctuations fully screening the Brillouin gain signal. On the other hand, in the case of the dual modulation set-up, the reflection is filtered out and the Brillouin gain can be measured with a good SNR.

S1.4 Experimental Brillouin gain calculation

Here, we use Eq. (17) to compute the Brillouin gain. The parameters are listed in Table S1.

Parameter name	Parameter description	Value
ς_P	Pump modulation depth	1.15
ς_S	Probe modulation depth	1.15
P_{P0}	Pump power at the input of the HCF (inside the HCF)	7.8 dBm
$P_{S,\text{det}}$	Probe power at the photodetector	-7.5 dBm
$f_P/2$	Pump modulation frequency	714.623 kHz
$f_S/2$	Probe modulation frequency	752.123 kHz
f_Δ	Detection frequency	75 kHz
α	HCF optical attenuation (including the 0.5 dB CO_2 absorption)	5.99 km^{-1}
n_g (41 bar)	HCF group refractive index	1.01804
ρ_{pd}	Photodetector power-to-voltage conversion factor	3.75 V/mW
α_F	Voltage attenuation factor due to the band-pass filter	0.827
$V_{s,\text{det}}$ (41 bar)	Lock-in amplifier voltage corresponding to the peak Brillouin gain	60.8 mW

Table S1: **Parameters used for computation of the Brillouin gain from the dual intensity modulation system response.** Note that the values of n_g and $V_{s,\text{det}}$ are given at 41 bar CO_2 -filled HCF as an example, and the pump and probe power are the time-averaged values.

Using these values along with Eqs. (12) and (18), we can compute $L_{\text{eff}} = 43.21 \text{ m}$, $\|\zeta_2\| = 0.657$. We now add α_F to Eq. (17) and rewrite it to obtain the expression of the Brillouin gain:

$$g_B = \frac{(1 - J_0(2\varsigma_S))(1 - J_0(2\varsigma_P)) \cdot V_{s,\text{det}}}{2J_2(2\varsigma_S)J_2(2\varsigma_P)\rho_{\text{pd}}P_{S,\text{det}}P_{P0}L_{\text{eff}}\alpha_F\|\zeta_2\|}. \quad (20)$$

By evaluating this equation using values for all parameters, we obtain $g_B = 1.68 \text{ m}^{-1}\text{W}^{-1}$ for 41 bar CO_2 , which is in good agreement with our Brillouin amplification and lasing measurements.

S2 Detailed experimental set-up for signal amplification

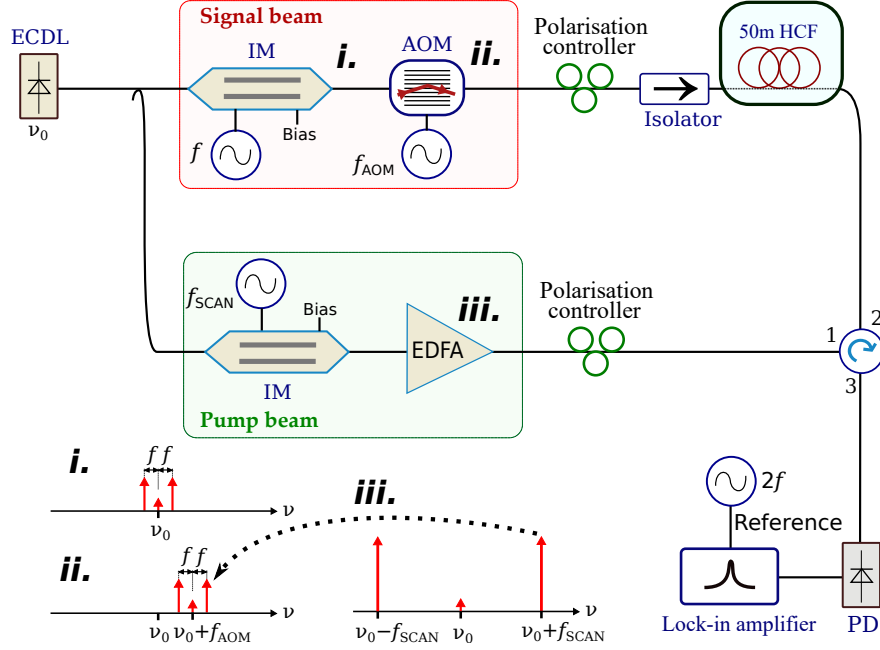


Figure S3: **Detailed experimental set-up for the signal amplification measurement.** ECDL, external-cavity diode laser; IM, intensity modulator; AOM, acousto-optic modulator; EDFA, erbium-doped fibre amplifier; PD, photodetector.

Parameter description	Value
HCF attenuation (including the 0.5 dB CO ₂ absorption)	5.99 km ⁻¹
Signal power at the input of the HCF (inside the HCF)	-34 dBm
Signal modulation frequency f	37.5 kHz
Lock-in amplifier detection frequency	75 kHz
Lock-in amplifier, signal power (average optical power) to voltage transfer coefficient	5.36 V/mW

Table S2: **Experimental details for signal amplification measurement.**

The detailed experimental set-up used for signal amplification measurements is shown in Fig. S3. Pump and probe (signal) beams are both from the same external-cavity diode laser. The pump light was generated by a Mach-Zehnder electro-optic modulator (with carrier-suppressed bias set-up) at modulation frequency f_{SCAN} and then amplified by an erbium-doped fibre amplifier. The signal goes through an intensity modulator at frequency $f=37.5$ kHz (carrier-suppressed bias, hence the power is modulated at frequency $2f = 75$ kHz) and then is frequency blue-shifted by an acousto-optic modulator ($f_{\text{AOM}} = +110$ MHz), in order to break the pump sideband symmetry. Therefore, only one pump sideband is used for the Brillouin interaction (here, only the higher-frequency sideband of the pump beam interacts with the signal). The injected signal power (average power) is -34 dBm, which is more than 40 dB smaller than the pump power, hence satisfying the small-signal amplification condition (i.e. absence of pump depletion).

By scanning the detuning frequency ($f_{\text{SCAN}} - f_{\text{AOM}}$) across the Brillouin frequency shift, we can measure the Brillouin amplification spectra as a function of the pump-signal detuning frequency using different pump powers. Here, the signal modulation frequency, $2f$, is much smaller than the linewidth of the Brillouin gain spectrum at 41-bar CO₂ (i.e. 3.65 MHz). This means that the two probe sidebands have the same Brillouin amplification coefficient. The output signal (inside the HCF before entering the output SMF) can be expressed as: $P_S(L) = P_S(0) \exp(P_{P0} g_B \mathcal{L}_I L_{\text{eff}} - \alpha L)$. By measuring the output signal (at 75 kHz) with

a lock-in amplifier and converting the voltage to optical power, we obtain the output signal power. The signal amplification is calculated as the ratio between the output signal power and the input signal power.

S3 Detailed experimental set-up for distributed temperature sensing

The experimental set-up we used is shown in Fig. S4. It is essentially a combination of a Brillouin optical correlation-domain analyser (BOCDA) based on phase modulation [3] with a dual-intensity modulation, presented in section S1, in order to filter out the pump reflection at the coupling interface. An intensity modulator generates two sidebands for the pump beam, used for the scanning. An AOM placed on the probe line shifts the probe frequency and thus breaks the pump sideband symmetry. Therefore, only one pump sideband is necessary for the scanning. The other unused sideband is not filtered but does not interfere in any way with the measurement. Polarisation is handled by placing a polarisation scrambler on the pump line. When the pseudo-random bit sequence (PRBS) generator is turned on, the random phase modulation applied to both pump and probe beams allows the acoustic waves to grow only in a precise location inside the fibre in which the phase of both pump and probe beams correlates and, thus, enables the experimental set-up to be used for distributed temperature sensing.

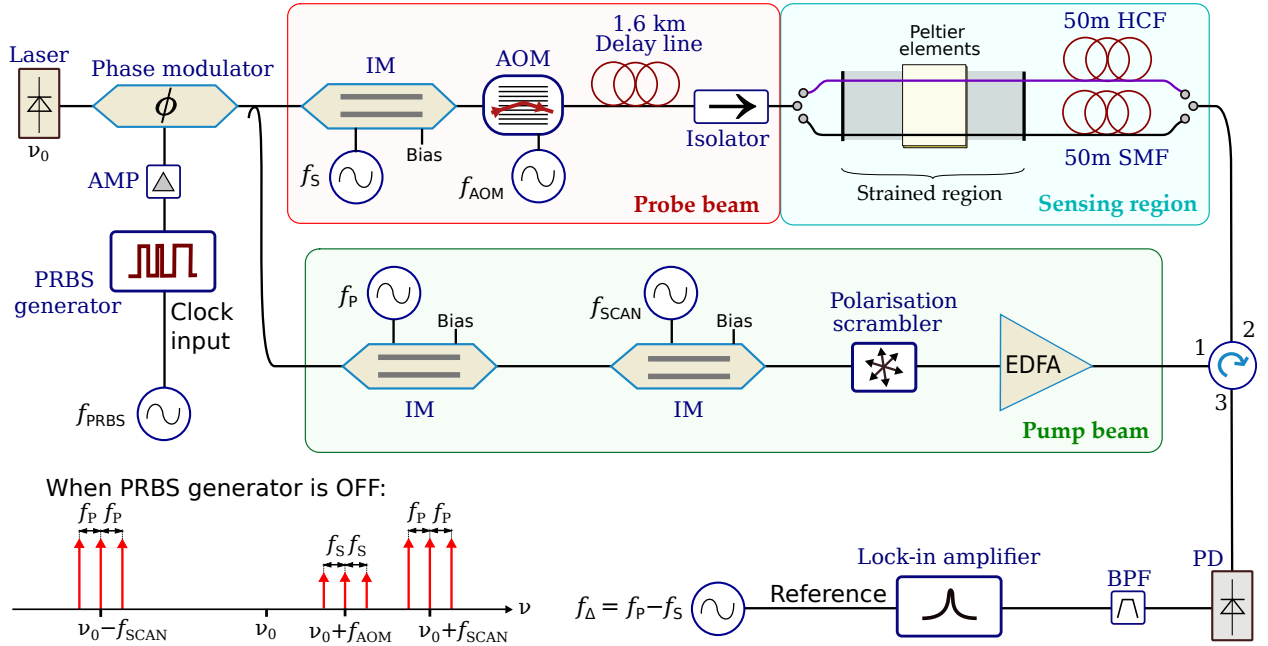


Figure S4: **Experimental set-up for distributed temperature sensing in a gas-filled HCF by implementing a BOCDA.** The implementation is a combination of BOCDA technique with the dual intensity modulation method (see text). Note that the three radio-frequency sources generating the frequencies f_P , f_S and f_Δ are synchronised to the same frequency standard. PRBS, pseudo-random bit sequence; AOM, acousto-optic modulator; IM, intensity modulator; EDFA, erbium-doped fibre amplifier; PD, photodetector; AMP, radio-frequency amplifier; BPF, band-pass filter.

S3.1 Dual intensity modulation implementation

The pump and probe are intensity-modulated with a RF modulation frequency of $f_P = 1$ MHz and $f_S = 1.075$ MHz, respectively, so that the frequency difference is $f_\Delta = f_P - f_S = 75$ kHz. The modulator bias configuration was tuned to the quadrature point, as illustrated in the spectrum of Fig. S4.

S3.2 PRBS generator

The PRBS generator reference clock f_{PRBS} was set to 11.7 GHz for HCF and to 4.5 GHz for SMF, leading to a bit duration τ_b of 85.5 ps and 222.2 ps, respectively. These frequencies were experimentally chosen as the highest frequencies for which our system still gave a reasonable signal-to-noise ratio ($\text{SNR} > 10$). The resulting spatial resolutions, computed as the inverse of the bit duration, were 1.28 cm and 2.32 cm for HCF and SMF respectively. The exact spatial resolutions are slightly higher (i.e. smaller length) than these values [4]. The PRBS sequence length N_{PRBS} was chosen as $N_{\text{PRBS}} = 2^{15} - 1$ such that the sequence length (420 m and 760 m for HCF and SMF, respectively) is large enough to cover the whole fibre length.

S3.3 Phase modulator

For proper functioning of the system, when the PRBS generator outputs a bit '1', a phase shift precisely equal to π has to be reached as fast as possible to avoid unwanted activation of acoustic wave in the fibre at specific locations corresponding to the switching of the PRBS sequence [4]. Hence, a low V_π ($V_\pi \approx 4$ V), high frequency (20 GHz) phase modulator was used in this experiment.

S3.4 Correlation location scanning

In order to adjust the optical path length difference, an optical delay-line able to delay an optical signal up to a time $\tau = L \cdot n/c$, where L is the measurement fibre length, would be required. Building such a delay-line is very challenging. Thus, another option is commonly adopted. This alternative method takes advantage of the fact that the total duration of the PRBS sequence, and thus the time at which the next sequences will start, depends on the bit duration. This technique consists of adding a fixed delay-line, i.e. an optical fibre of length $L_{\text{dl}} > N_{\text{PRBS}} \cdot \tau_b \cdot n_g/c$ (in our case, $L_{\text{dl}} = 1.6$ km) in either the probe or pump path and slightly tuning the PRBS bit duration to shift the time at which the next sequences will start. The change of the correlation peak location Δz_{cp} as a result of a slight change of the PRBS clock frequency Δf_{PRBS} is found to be given by [5]:

$$\Delta z_{\text{cp}} = \frac{1}{2} \frac{\Delta f_{\text{PRBS}}}{f_{\text{PRBS}}} \cdot L_{\text{dl}}. \quad (21)$$

Thus, in our case, the total change of the PRBS clock frequency Δf_{PRBS} required to scan the whole fibre is: $\Delta f_{\text{PRBS}}/f_{\text{PRBS}} = 6\%$. This change of the PRBS clock frequency results in a 6% change in the spatial resolution, which can be neglected here.

S3.5 Pump power

The pump power, before entering either the HCF or the SMF, was set to 100 mW. In the case of the HCF, further increase in the power did not lead to an increase in the SNR. The power is estimated to be limited by the reflection of the amplified spontaneous emission noise from the erbium-doped fibre amplifier, directly entering into the photodetector.

S3.6 Probe signal acquisition

Probe signal was recorded by using a standard detector ($\text{NEP} = 20 \text{ pW}/\sqrt{\text{Hz}}$) followed by a 75 kHz bandpass RF filter to select only the signal of interest. Measurement spectra were recorded using a 7.8 Hz equivalent noise bandwidth (the lock-in amplifier was set to 10 ms time constant with 24 dB/octave filter slope) and their peak gain frequency were estimated using the quadratic fitting described in section S3.7.

S3.7 Scanning, quadratic fitting and repeatability estimation

The scanning steps for HCF and SMF was 0.5 MHz and 1 MHz, respectively.

The quadratic fitting algorithm first applies a low-pass filter to the Brillouin gain data points and takes the maximum value in order to find the approximate peak position. Then, it keeps 17 original data points on each side from the approximate peak data point and discards the remaining data points. Note that these

data points are the original data (without low-pass filtering). Finally, it performs a least-square quadratic fitting on these original data points.

The repeatability for the HCF and the SMF is computed as the average along 21 position points of the standard deviations of 8 measurements, previously fitted with the aforementioned quadratic fitting.

S3.8 Test bench

In order to demonstrate the absence of strain sensitivity and to perform a fair comparison with the standard single-mode fibre, a dedicated test bench was built, which enables us to apply both strain and temperature changes at the same fibre location. The ends of both our 50-m-long HCF and of a 50-m-long ITU G.652 single-mode fibre used for comparison are placed inside this test bench, which consists of two parts:

- Temperature stage. The fibres are "sandwiched" between two 4-cm-long Peltier elements, placed below and above the two fibres, respectively. The thermal conductivity between the Peltier elements and the fibres is ensured by the presence of thermal paste. Furthermore, two metallic radiators are placed on the other side of each Peltier element to provide/dissipate heat from/to the environment. In addition, a fan forces the flow of air through these radiators in order to ensure a sharp temperature transition. A PT-1000 thermometer was placed in the thermal paste between the Peltier elements at the vicinity of the fibres and a proportional-integral (PI) controller was used for precise temperature stabilisation.
- Strain stage. The previously described temperature stage is placed in the middle of a 15-cm-long strain stage. On one side, the fibres are glued onto a fixed metallic plate while on the other side, they are glued onto a displacement stage. Note that the coating of the two fibres was removed at the gluing points.

A picture of this test bench is provided in Fig. S5, including the various lengths. Note that the fan is not visible in the picture.

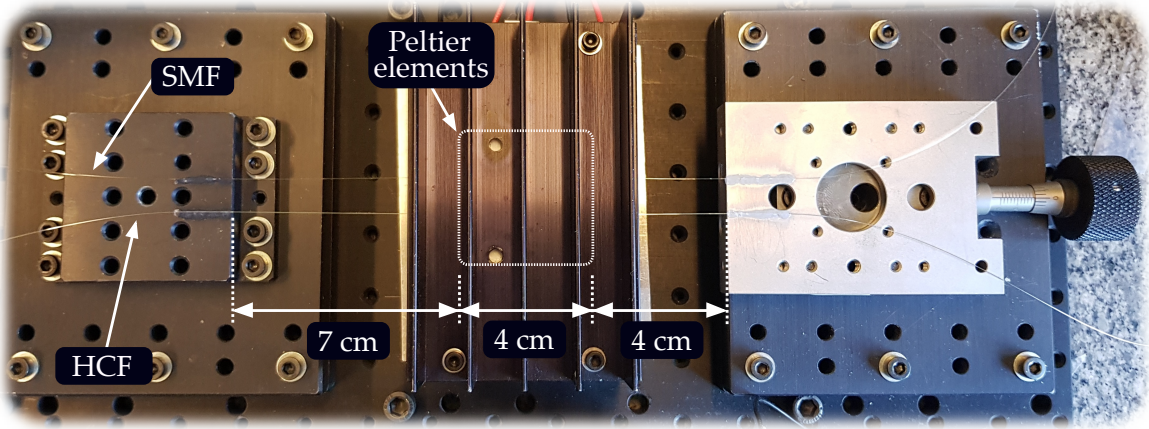


Figure S5: **Test bench for distributed temperature sensing.** Test bench to demonstrate the absence of strain sensitivity. A 4-cm-long temperature stage is placed in the middle of a 15-cm-long strain stage, allowing to apply strain and temperature changes in the same region of the fibres. Both SMF and HCF cross the test bench parallel to each other and are placed close to each other for a fair comparison.

S4 Theoretical calculation of the Brillouin gain

The acousto-optic overlap effective area is given by [8]:

$$A_{\text{eff}}^{\text{ao}} = \left[\frac{\langle f^2(x, y) \rangle}{\langle \xi(x, y) f^2(x, y) \rangle} \right]^2 \langle \xi^2(x, y) \rangle, \quad (22)$$

Parameter name	Parameter description	Value (for CO ₂ at 41 bar)
$A_{\text{eff}}^{\text{ao}}$	Acousto-optic overlap effective area	80 μm^2
η_s	Shear viscosity [6]	1.5×10^{-5} Pa·s
η_b	Bulk viscosity [7]	4×10^{-6} Pa·s
κ	Thermal conductivity	$0.01662 \text{ W} \cdot \text{m}^{-1} \text{K}^{-1}$
C_P	Specific heat at constant pressure	$846 \text{ J} \cdot \text{kg}^{-1} \text{K}^{-1}$
ρ	Gas density	72.77 kg/m^3
γ	Heat capacity ratio (adiabatic index)	1.3
n	Refractive index of the gas	1.01804
T	Temperature	298 K
v_a	Acoustic velocity	243.6 m/s

Table S3: **Detailed parameters for the theoretical calculation of the Brillouin gain.** Note that ideal gas model was assumed for the calculation of C_P , ρ and γ . More complex calculations taking into account non-ideal gas models do not significantly alter the values.

where $f^2(x, y)$ and $\xi(x, y)$ are the transverse optical intensity profile and acoustic pressure profile of the fibre, respectively, and where the operator $\langle \dots \rangle$ performs an integration over the entire fibre cross-section. We use the numerical simulation results shown in Figs. 1(c) and (d) in the main manuscript and make overlap integration to obtain the acousto-optic overlap effective area: $A_{\text{eff}}^{\text{ao}} = 80 \mu\text{m}^2$. By plugging all the parameters of 41-bar CO₂ into Eq. (1) in the main manuscript, we can calculate the theoretical Brillouin gain to be $1.86 \text{ m}^{-1} \text{W}^{-1}$, which is very close to the measured Brillouin gain $1.68 \text{ m}^{-1} \text{W}^{-1}$. By inserting all the parameters into Eq. (6) in the main manuscript, we obtain a Brillouin linewidth of 4.3 MHz, which is also close to the measured linewidth 3.65 MHz.

S5 Calculation of Raman gain coefficient

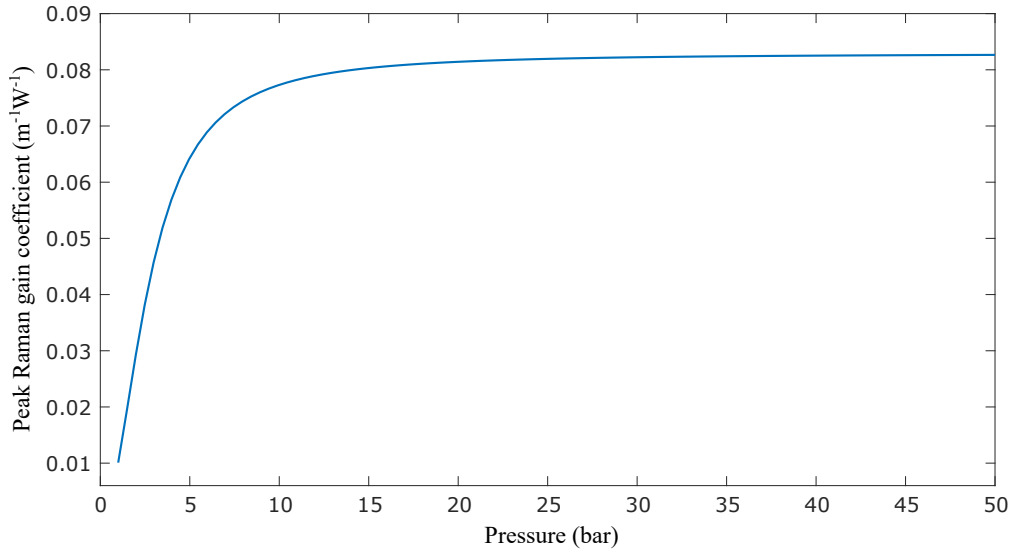


Figure S6: **Raman gain coefficient as a function of hydrogen pressure at a wavelength of 1.55 μm and room temperature (Q(1) vibrational transition).**

So far, hydrogen gas shows the highest Raman gain (at a detuning frequency of 125 THz for the Q(1) vibrational transition) of any gas [9]. The peak plane-wave steady-state Raman-gain coefficient, g_R (in units of cm/W), for the Q(1) transition for pump-laser wavelengths from 190 nm to 2 μm , densities of 1-100

amagats, at room temperature (298 K) is given as [10, 11]:

$$g_R = 9.37 \times 10^6 \cdot \frac{(52\rho/\Delta\nu)(\nu_p - 4155)}{(7.19 \times 10^9 - \nu_p^2)^2}, \quad (23)$$

where ρ is the density in amagats, $\Delta\nu$ is the Raman linewidth in MHz, given by $\Delta\nu = (309/\rho) + 51.8\rho$ at room temperature, ν_p is the pump laser frequency in inverse centimetres. This means when the density is above 9 amagats, $\Delta\nu \approx 51.8\rho$ MHz. At room temperature, a pressure of 1 amagat corresponds to 1.1 bar. As a result, the peak Raman gain is independent of density (i.e it is saturated) when the pressure is above 10 bar because the Raman linewidth is proportional to the pressure (pressure broadening region, caused by the onset of inelastic rotational collisions [12]). By substituting this pressure into Eq. (23), we can compute the Raman gain (in units of cm/W) as a function of pressure. The saturated maximum Raman gain coefficient is calculated as $4.2 \times 10^{-12} \text{ m/W}$ at $1.55 \text{ }\mu\text{m}$. Assuming the use of the same HCF with a core diameter of $10.9 \text{ }\mu\text{m}$ and an optical effective mode field area of $51 \text{ }\mu\text{m}^2$ (calculated with COMSOL), the peak Raman gain coefficient (in units of $\text{m}^{-1}\text{W}^{-1}$) as a function of pressure is plotted in Fig. S6. The highest Raman gain for more than 10 bar (e.g. 41 bar) hydrogen is $0.08 \text{ m}^{-1}\text{W}^{-1}$, which is more than 20 times smaller than the Brillouin gain in gas demonstrated in this paper.

S6 Acoustic velocity in CO_2 at different gas pressures

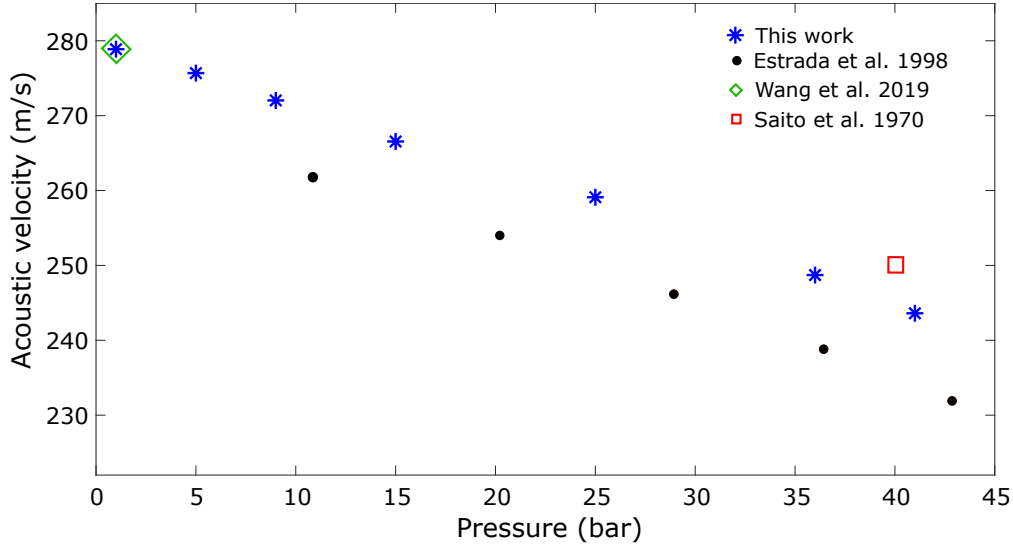


Figure S7: **Acoustic velocity in CO_2 at different gas pressures.**

We measured the Brillouin gain spectrum at different gas pressures. The pump-probe frequency detuning at the peak gain is called Brillouin frequency shift and is given by [6]:

$$\nu_B = \frac{2n_{\text{eff}}v_a}{\lambda_P}, \quad (24)$$

where n_{eff} is the effective refractive index of the optical mode, v_a is the acoustic velocity and λ_P is the pump wavelength. As an approximation, we used the gas refractive index n as the effective refractive index n_{eff} . We can derive the measured acoustic velocity (shown by blue stars in Fig. S6) from the Brillouin frequency shift by using Eq. (24). The black dots in Fig. S6 is the measured results for low frequency acoustic waves (several kilohertz) from Ref. [13]. Our results show a very similar trend. The mismatch of the absolute value is probably due to the different values of the bulk modulus at different acoustic frequencies (our frequency range is $\sim 320 \text{ MHz}$), possibly caused by translational-vibrational relaxation processes, since CO_2 is a polyatomic gas. The green diamond in Fig. S6 represents the measured acoustic velocity for a 500

MHz acoustic wave at 1 bar from Ref. [6]. This value matches well with our measurement. The red square in Fig. S6 shows the measured acoustic velocity at 40 °C from Fig. 5 in Ref [14]. This value is a little bit higher than our result, probably because their temperature is higher than in our experiments.

S7 Axial strain finite-element simulation

An axial strain applied on the fibre will lead to the following effects:

- Due to the Poisson effect, the honey-comb structure will be distorted, modifying the effective refractive index of the optical mode.
- In particular, the holes will shrink and the fibre will elongate, leading to a change in the volume available for the gas along the fibre.
- The silica refractive index will change due to the photo-elastic effect, leading to a change in the effective refractive index of the optical mode.

In order to quantify these effects, a finite-element simulation has been performed. To this end, deformations of a 3D slice of the HCF subject to an axial strain, ϵ , were computed. The deformations in the cross-section plane have subsequently been used to compute the resulting change in the effective refractive index n_{eff} . Although this computation was performed assuming 40 bar gas pressure in the holes, the results only weakly depend on the gas pressure. Figure S7(a) shows the deformed geometry (white lines) compared to the original geometry (black lines) for a hypothetical strain of 20%, as well as the normalised electric field for one fundamental mode in the deformed structure. Figure S7(b) shows the evolution of the effective refractive index, n_{eff} , relative to the effective refractive index in the undeformed case, $n_{\text{eff},0}$, as a function of strain, from 0 up to 2%. The red trace shows the contribution of the photo-elastic effect while the blue trace shows the contribution of the structure deformation (as shown in Fig. S7(a)). These two contributions show a linear evolution equal to: $\partial n_{\text{eff}}/\partial \epsilon = -2.4 \times 10^{-3}$ and $\partial n_{\text{eff}}/\partial \epsilon = +7.08 \times 10^{-4}$ for the photo-elastic effect and for the deformation, respectively. We can see that the photo-elastic effect dominates and is partly compensated by the contribution of the deformation. The black dotted line shows the total evolution of n_{eff} as a function of the applied axial strain and has a linear value of: $n_{\text{eff}}/\partial \epsilon = -1.7 \times 10^{-3}$.

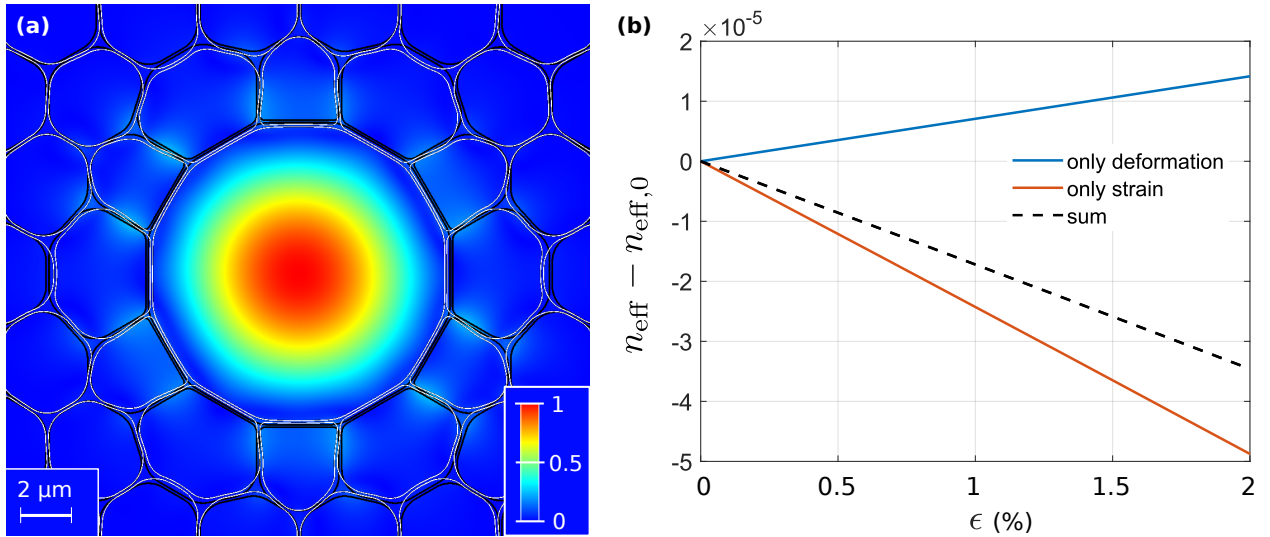


Figure S8: **Simulation of the deformation of the HCF's cross-section in response to an axial strain.** (a) Normalised electric field magnitude of one of the two fundamental modes (optical wavelength: 1.55 μm) in the case of a hypothetical axial strain of 20%. White lines draw the deformed structure while black lines draw the original, undeformed structure. (b) Evolution of the effective refractive index, n_{eff} , as a function of the strain and relative to the effective refractive index in absence of strain, $n_{\text{eff},0}$. The blue line accounts only for the structure deformation, the red line accounts only for the photo-elastic effect and the dotted black line accounts for the total evolution (i.e. the sum of these two contributions).

We are now in position to estimate the local change in the Brillouin frequency shift due to an axial strain along the HCF. The change of the Brillouin frequency shift due to an axial strain ϵ can be written as:

$$\frac{d\nu_B}{d\epsilon} = \frac{\nu_B}{n} \frac{\partial n}{\partial \epsilon} + \frac{\nu_B}{V_a} \frac{\partial V_a}{\partial \epsilon}. \quad (25)$$

Considering the 40 bar CO₂ Brillouin frequency shift of 320 MHz and $n \approx 1$, the first term can be directly evaluated to:

$$\frac{\nu_B}{n} \frac{\partial n}{\partial \epsilon} = -544 \text{ MHz}/\mu\epsilon. \quad (26)$$

In order to evaluate the second term, we consider that the fibre, of length L , is axially strained over a length l . In these conditions, the total change in the gas pressure P is:

$$\frac{\Delta P}{P} = -\frac{\Delta V}{V} = -\epsilon(1 - 2\kappa) \frac{l}{L}, \quad (27)$$

where we considered the change in volume of a cylinder of volume V_c , stretched by a strain ϵ_c , that can be expressed as: $\Delta V_c/V_c = \epsilon_c(1 - 2\kappa)$, with κ being the Poisson ratio. Taking as an extreme example a 40-bar gas-filled 50-m-long fibre whose entire length is strained by an axial strain of 2% (i.e. 1 meter elongation), the total pressure change would be: $\Delta P = -0.5$ bar. As the pressure-dependent Brillouin frequency was found to be of ≈ -1 MHz/bar, the total change in the Brillouin frequency due to the gas pressure variation would be of $+0.5$ MHz. In addition, the change in the Brillouin frequency due to the effective refractive index variation would be of -10.8 kHz. We can see that these two effects have an opposite sign and partly compensate for each other. For example, if we consider the same example but with the strain applied along a 20 centimeter-long portion of the fibre only, the change in the Brillouin frequency due to the gas pressure variation would be 10 kHz and would almost perfectly compensate for the change in the Brillouin frequency due to the effective refractive index variation. In summary, we demonstrated that the change in the Brillouin frequency due to an applied axial strain can be neglected in normal operation.

S8 Response of a Mach-Zehnder intensity modulator

S8.1 Introduction

In this section, we discuss the Mach-Zehnder modulator and derive an expression for the output intensity in the special case of a RF sinusoidal modulation. A typical Mach-Zehnder modulator consists of a lithium niobate (LiNbO₃) substrate in which optical waveguides are imprinted. Metallic electrodes are subsequently deposited on top of the substrate. A top view and a cross-section of a typical Mach-Zehnder modulator is shown in Fig. S9(a) and (b) respectively [15].

The input waveguide is split into two arms and the top electrodes are used to induce an electric field into the two arms. Thanks to Pockels effect, the induced electric field leads to a slight increase in the refractive index to one arm and a slight decrease in the other arm. The two waveguides are then merged into one output waveguide again, resulting in an interference of the two optical fields. The extinction ratio is a parameter measuring the intensity ratio between constructive interference and destructive interference and its value is typically ≈ 25 dB (however, in the modulators used in this work, it was larger than 35 dB). Figure S9(c) shows the normalised output intensity (neglecting insertion loss) as a function of the applied RF voltage, following a cosine variation. The voltage change required to go from a constructive interference to a destructive interference is called V_π .

In order to simplify the calculation, we assume a perfect modulator as possessing the following characteristics:

- The modulator is lossless. However, insertion loss can be easily added by simple multiplication of the results with a loss factor.
- The modulator has an infinite bandwidth. This essentially means that the modulation frequency is much smaller than the modulator cut-off bandwidth and simplifies the derivation by ignoring the effects of a finite bandwidth.
- The modulator has exactly equal arm lengths. While never the case in reality, compensation for unequal arm lengths and temperature drifts can be easily done by adjusting the modulator's bias voltage.

- In the case of a destructive interference, no light intensity is present at the output (infinite extinction ratio).

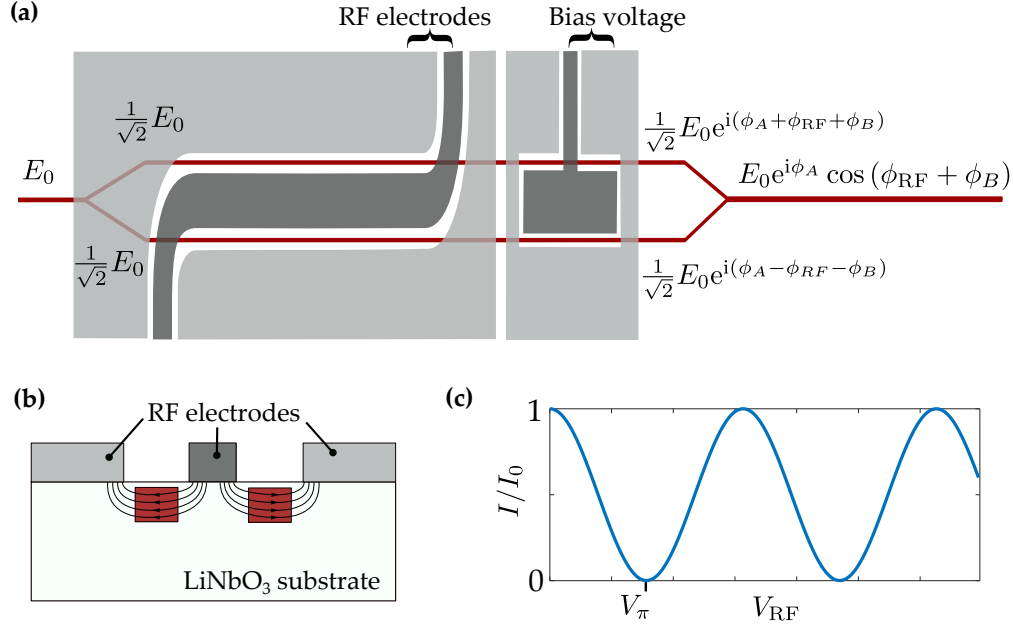


Figure S9: **Mach-Zehnder modulator.** (a) Top view of a typical Mach-Zehnder modulator. The waveguides are drawn in red and the electrodes in gray (dark gray for the signal electrode and light gray for the ground electrode). Light propagates from left to right. Expressions indicate the electric field at various positions. (b) Cross-section of a typical Mach-Zehnder modulator showing the lithium niobate (LiNbO_3) substrate, the waveguide of the two arms in red and the electrodes in gray (dark gray for the signal electrode and light gray for ground electrode). The arrows show the orientation of the electric field crossing the waveguides when the RF voltage is positive. (c) Normalised output light intensity as a function of the RF voltage, V_{RF} , following a cosine function.

As shown in Fig. S9(a), in presence of an input electric field E_0 , the electric field at the output of the modulator reads:

$$E = E_0 e^{i\phi_A} \cos(\phi_{\text{RF}} + \phi_B), \quad (28)$$

where $e^{i\phi_A}$ is the phase shift induced by the light propagation across the modulator, $\phi_{\text{RF}} = \pi V_{\text{RF}}/2V_\pi$ is the phase shift induced when applying a RF voltage $V_{\text{RF}}(t)$ to the electrodes and ϕ_B is the bias phase shift induced when applying a certain voltage to the bias port. Since $e^{i\phi_A}$ is a common phase shift that is simply due to transmission across the device, we disregard it from now on.

We now apply a sinusoidal RF voltage of frequency $\Omega/2\pi$ and of amplitude V :

$$V_{\text{RF}}(t) = V \sin(\Omega t). \quad (29)$$

The RF phase shift is:

$$\phi_{\text{RF}} = \frac{\pi}{2} \frac{V_{\text{RF}}(t)}{V_\pi} = \varsigma \sin(\Omega t), \quad (30)$$

where $\varsigma = \pi V/2V_\pi$ is called the modulation depth. Inserting Eq. (30) into Eq. (28) and applying Jacobi-Anger's identity, we obtain:

$$\begin{aligned} E &= E_0 \text{Re} \left\{ e^{i\varsigma \sin \Omega t} e^{i\phi_B} \right\} = E_0 \text{Re} \left\{ e^{i\phi_B} \sum_n J_n(\varsigma) e^{in\Omega t} \right\} \\ &= E_0 \sum_n J_n(\varsigma) \cos(n\Omega t + \phi_B), \end{aligned} \quad (31)$$

where J_n are the Bessel functions of the first kind and n is a scalar going from $-\infty$ to $+\infty$. We will use this equation to derive an expression for the output intensity, as observed when connecting the modulator output to a photodetector.

S8.2 Intensity at a photodetector

We now calculate the output intensity $I = \|E\|^2 / 2\eta$, where η is the medium impedance. We define $I_0 = \|E_0\|^2 / 2\eta$ as the input light intensity and take the magnitude squared of Eq. (31):

$$\begin{aligned} I(t) &= I_0 \sum_n \sum_m J_n(\varsigma) J_m(\varsigma) \cos(n\Omega t + \phi_B) \cos(m\Omega t + \phi_B) \\ &= \frac{1}{2} I_0 \sum_n \sum_m J_n(\varsigma) J_m(\varsigma) [\cos((n+m)\Omega t + 2\phi_B) + \cos((n-m)\Omega t)]. \end{aligned} \quad (32)$$

At this point, it is useful to rearrange the terms by defining the following variable change: $p = n + m$ and $q = n - m$. As illustrated in table S4, this procedure is equivalent to switching from a horizontal/vertical indices scanning to a diagonal one. Note that p and q should have the same parity: when p is even, q also has to be even and when p is odd, q also has to be odd. We thus separate the sum into two parts; one for odd values of p and q and one for even values of p and q . The sums are thus rearranged and written as:

Table S4: Illustration of the variables change: $p = n + m$ and $q = n - m$. Original horizontal and vertical scanning for n and m indices of the summation is changed to a diagonal scanning for p and q . Note that although the indices shown run from -3 to 3 , the actual sum is infinite.

$n + m :$								$n - m :$							
n								n							
	-3	-2	-1	0	1	2	3		-3	-2	-1	0	1	2	3
-3	-6	-5	-4	-3	-2	-1	0	-3	0	1	2	3	4	5	6
-2	-5	-4	-3	-2	-1	0	1	-2	-1	0	1	2	3	4	5
-1	-4	-3	-2	-1	0	1	2	-1	-2	-1	0	1	2	3	4
m 0	-3	-2	-1	0	1	2	3	m 0	-3	-2	-1	0	1	2	3
1	-2	-1	0	1	2	3	4	1	-4	-3	-2	-1	0	1	2
2	-1	0	1	2	3	4	5	2	-5	-4	-3	-2	-1	0	1
3	0	1	2	3	4	5	6	3	-6	-5	-4	-3	-2	-1	0
p	0	1	2	3	4	5	6	q	-6	-5	-4	-3	-2	-1	0

$$\begin{aligned} I(t) &= \frac{1}{2} I_0 \sum_p \sum_q J_{p+q}(\varsigma) J_{p-q}(\varsigma) [\cos(2p\Omega t + 2\phi_B) + \cos(2q\Omega t)] \\ &\quad + \frac{1}{2} I_0 \sum_p \sum_q J_{p+q+1}(\varsigma) J_{p-q}(\varsigma) [\cos((2p+1)\Omega t + 2\phi_B) + \cos((2q+1)\Omega t)]. \end{aligned} \quad (33)$$

We then use the following identities:

$$\begin{aligned}
\sum_q J_{p+q}(\varsigma) J_{p-q}(\varsigma) &= J_{2p}(2\varsigma) \\
\sum_p J_{p+q}(\varsigma) J_{p-q}(\varsigma) &= \begin{cases} 1, & q = 0 \\ 0, & \text{otherwise} \end{cases} \\
\sum_q J_{p+q+1}(\varsigma) J_{p-q}(\varsigma) &= J_{2p+1}(2\varsigma) \\
\sum_p J_{p+q+1}(\varsigma) J_{p-q}(\varsigma) &= 0,
\end{aligned} \tag{34}$$

which enable rewriting Eq. (33) as:

$$I(t) = \frac{1}{2} I_0 \left(1 + \sum_n J_n(2\varsigma) \cos(n\Omega t + 2\phi_B) \right). \tag{35}$$

In order to isolate the different frequency components, we can modify the result as follows:

$$\begin{aligned}
I(t) = \frac{1}{2} I_0 \left(1 + J_0(2\varsigma) \cos(2\phi_B) + \sum_{n=1}^{\infty} J_n(2\varsigma) \cos(n\Omega t + 2\phi_B) \right. \\
\left. + \sum_{n=1}^{\infty} (-1)^n J_n(2\varsigma) \cos(n\Omega t - 2\phi_B) \right),
\end{aligned} \tag{36}$$

where the relation $J_{-n}(\varsigma) = (-1)^n J_n(\varsigma)$ has been used. Using trigonometric relations and again separating odd and even frequencies, it follows that:

$$\begin{aligned}
I(t) = I_0 \left(\frac{1}{2} + \frac{J_0(2\varsigma)}{2} \cos(2\phi_B) \right. \\
- \sin(2\phi_B) \sum_{n=1}^{\infty} J_{2n-1}(2\varsigma) \sin((2n-1)\Omega t) \\
\left. + \cos(2\phi_B) \sum_{n=1}^{\infty} J_{2n}(2\varsigma) \cos(2n\Omega t) \right),
\end{aligned} \tag{37}$$

where the first line represents the DC part, the second line represents the odd harmonics and the third line represents the even harmonics. From this expression, four particular values of the bias ϕ_B can be distinguished:

- When $\phi_B = \pi/2 + z\pi$, $z \in \mathbb{Z}$, only the even harmonics are present and the DC value is low. This configuration is usually referred to as "carrier-suppressed".
- When $\phi_B = 0 + z\pi$, $z \in \mathbb{Z}$, only the even harmonics are present and the DC value is high. This configuration is usually referred to as "full-carrier".
- When $\phi_B = \pi/4 + z\pi$, $z \in \mathbb{Z}$, only the odd harmonics are present. This configuration is usually referred to as "quadrature point".
- When $\phi_B = 3\pi/4 + z\pi$, $z \in \mathbb{Z}$, only the odd harmonics are present. This configuration is also usually referred to as "quadrature point". The only difference with respect to the previous case is the presence of a π -phase shift for the output intensity modulation.

S8.3 Analysis of the three bias configurations

Carrier-suppressed configuration

When the bias is set so that $\phi_B = \pi/2 + z\pi$, $z \in \mathbb{Z}$, the output intensity contains only even multiples of the modulation frequency:

$$I(t) = I_0 \left(\frac{1}{2} - \frac{J_0(2\varsigma)}{2} - \sum_{n=1}^{\infty} J_{2n}(2\varsigma) \cos(2n\Omega t) \right). \tag{38}$$

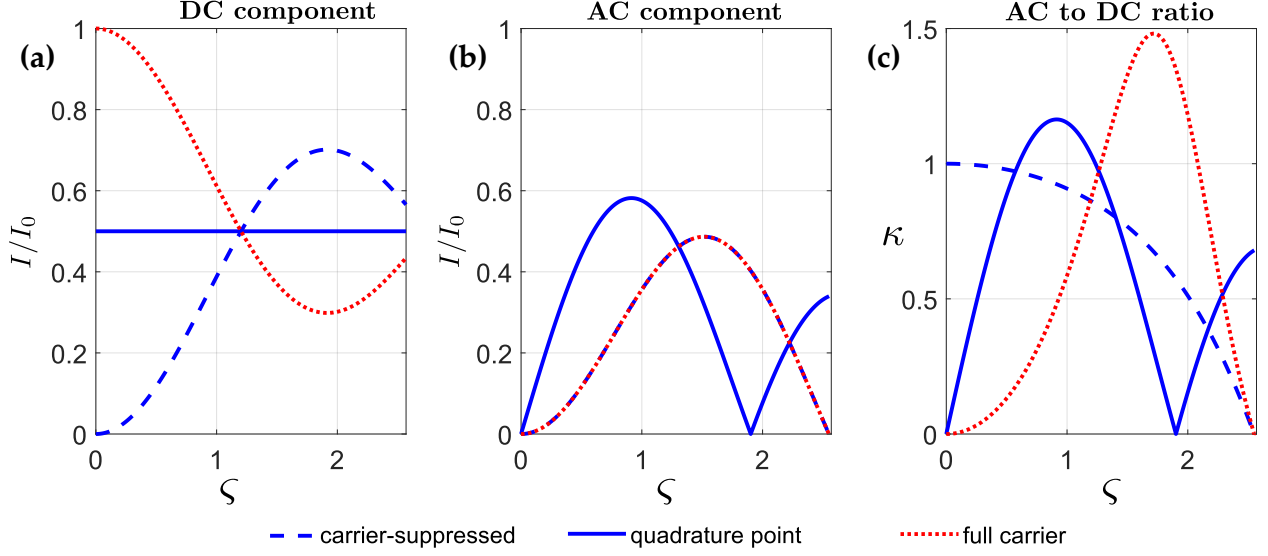


Figure S10: **DC and AC intensities.** (a) Evolution of the DC component of the modulator output intensity as a function of the modulation depth ς . (b) Evolution of the AC component of the modulator output intensity as a function of the modulation depth ς . (c) Evolution of the AC to DC ratio as a function of the modulation depth ς .

When the modulation depth ς is moderate (< 2), the sum can be approximated by keeping only the first term:

$$I(t) \cong I_{\text{det}} \left(1 - \kappa_S \cos(2\Omega t) \right), \quad (39)$$

where $I_{\text{det}} = I_0(1 - J_0(2\varsigma))/2$ is the time-averaged detected intensity and $\kappa_S = 2J_2(2\varsigma)/(1 - J_0(2\varsigma))$ is the ratio of the intensity at frequency 2Ω to the DC intensity. The evolution of this parameter as a function of the modulation depth is plotted in Fig. S10(c).

Quadrature point configuration

When the bias is set so that $\phi_B = \pi/4 + z\pi, z \in \mathbb{Z}$ or $\phi_B = 3\pi/4 + z\pi, z \in \mathbb{Z}$, the output intensity contains only odd multiples of the modulation frequency:

$$I(t) = \frac{1}{2} I_0 \left(1 \pm 2 \sum_{n=1}^{\infty} J_{2n-1}(2\varsigma) \sin((2n-1)\Omega t) \right), \quad (40)$$

where the sign in front of the sum depends on the choice of the bias points amongst the two cited above. When the modulation depth ς is moderate (< 2), the sum can be approximated by keeping only the first term:

$$I(t) \cong I_{\text{det}} \left(1 - \kappa_Q \sin(\Omega t) \right), \quad (41)$$

where this time $I_{\text{det}} = I_0/2$, which is the time-averaged detected intensity, is independent from the modulation depth. $\kappa_Q = 2J_1(2\varsigma)$ is the ratio of the intensity at frequency Ω to the DC intensity. The evolution of this parameter as a function of the modulation depth is plotted in Fig. S10(c).

Full carrier configuration

When the bias is set so that $\phi_B = 0 + z\pi, z \in \mathbb{Z}$, the situation is similar to the carrier-suppressed situation except that the DC component is higher and the modulation has a phase shift:

$$I(t) = I_0 \left(\frac{1}{2} + \frac{J_0(2\varsigma)}{2} + \sum_{n=1}^{\infty} J_{2n}(2\varsigma) \cos(2n\Omega t) \right). \quad (42)$$

When the modulation depth ς is moderate (< 2), the sum can be approximated by keeping only the first term:

$$I(t) \cong I_{\text{det}} \left(1 + \kappa_F \cos(2\Omega t) \right), \quad (43)$$

where $I_{\text{det}} = I_0(1 + J_0(2\varsigma))/2$ is the time-averaged detected intensity and $\kappa_F = 2J_2(2\varsigma)/(1 + J_0(2\varsigma))$ is the ratio of the intensity at frequency 2Ω to the DC intensity. The evolution of this parameter as a function of the modulation depth is plotted in Fig. S10(c).

Output intensity for the different carrier configurations

We now use the aforementioned expressions to compare the output intensities for each bias configuration. Figure S10(a) shows the evolution of the DC component of the Mach-Zehnder output intensity as a function of the modulation depth ς . Figure S10(b) shows the evolution of the AC component (at frequency Ω for the quadrature point, at frequency 2Ω for the full-carrier and carrier-suppressed configurations) of the Mach-Zehnder output intensity as a function of the modulation depth ς and Figure S10(c) plots the ratio of these two quantities (i.e. AC-to-DC intensity ratio), κ . It can be seen that the highest AC intensity among the three bias configuration is reached by the quadrature point. Moreover, for this bias configuration, the AC component peak appears at lower values of the modulation depth ς . In practice, the RF source output power is typically limited to ≈ 25 dBm and the V_π of a standard modulator reaches 7 V, so the modulation depth can typically reach a maximum value of $\varsigma \approx 1.2$. Hence, the quadrature point bias configuration is ideal to achieve the highest modulation intensity. The parameter κ is experimentally useful to quickly estimate the optical power at the modulation frequency by simply measuring the DC optical power using a power-meter.

Bibliography

- [1] Grubbs, W. T. & MacPhail, R. A. High resolution stimulated Brillouin gain spectrometer. *Review of Scientific Instruments* **65**, 34–41 (1994).
- [2] Boyd, R. W. *Nonlinear optics*, 436–440 (Elsevier, 2003).
- [3] Denisov, A., Soto, M. A. & Thévenaz, L. Going beyond 1000000 resolved points in a Brillouin distributed fiber sensor: theoretical analysis and experimental demonstration. *Light: Science & Applications* **5**, e16074 (2016).
- [4] Denisov, A. Brillouin dynamic gratings in optical fibres for distributed sensing and advanced optical signal processing (2015). URL <http://infoscience.epfl.ch/record/212806>.
- [5] Chow Ming Chia, D. Distributed analyses using distinct classes of Brillouin scatterings in optical fibres (2018). URL <http://infoscience.epfl.ch/record/261229>.
- [6] Wang, Y., Ubachs, W. & Van De Water, W. Bulk viscosity of CO₂ from Rayleigh-Brillouin light scattering spectroscopy at 532 nm. *The Journal of Chemical Physics* **150**, 154502 (2019).
- [7] Pan, X., Shneider, M. N. & Miles, R. B. Power spectrum of coherent Rayleigh-Brillouin scattering in carbon dioxide. *Physical Review A* **71**, 045801 (2005).
- [8] Kobayakov, A., Sauer, M. & Chowdhury, D. Stimulated Brillouin scattering in optical fibers. *Advances in Optics and Photonics* **2**, 1–59 (2010).
- [9] Mridha, M. K., Novoa, D., Hosseini, P. & Russell, P. S. J. Thresholdless deep and vacuum ultraviolet Raman frequency conversion in hydrogen-filled photonic crystal fiber. *Optica* **6**, 731–734 (2019).
- [10] Bischel, W. K. & Dyer, M. J. Wavelength dependence of the absolute Raman gain coefficient for the Q(1) transition in H₂. *Journal of the Optical Society of America B* **3**, 677–682 (1986).
- [11] Russell, P. S. J., Hölzer, P., Chang, W., Abdolvand, A. & Travers, J. C. Hollow-core photonic crystal fibres for gas-based nonlinear optics. *Nature Photonics* **8**, 278–286 (2014).
- [12] Bischel, W. K. & Dyer, M. J. Temperature dependence of the raman linewidth and line shift for the Q(1) and Q(0) transitions in normal and para-H₂. *Physical Review A* **33**, 3113 (1986).
- [13] Estrada-Alexanders, A. & Trusler, J. Speed of sound in carbon dioxide at temperatures between (220 and 450) K and pressures up to 14 MPa. *The Journal of Chemical Thermodynamics* **30**, 1589–1601 (1998).
- [14] Saito, T. T., Peterson, L. M., Rank, D. H. & Wiggins, T. A. Measurement of hypersound speed in gases by stimulated Brillouin scattering. *Journal of the Optical Society of America* **60**, 749–755 (1970).
- [15] Introduction to iXBlue Mach-Zehnder modulators bias controllers. https://photonics.ixblue.com/sites/default/files/2018-07/Introduction_To_Photline_MBC_2016_1.pdf. Accessed: 2019-07-29.